ITC 4/54
Information Technology and Control
Vol. 54 / No. 4/ 2025
pp. 1459-1479
DOI 10.5755/j01.itc.54.4.42585

An Efficient Algorithm for Distinguishing Triple Negative Breast Cancer with Ultrasound Image and High-dimensional Radiomics Data

Received 2025/08/19 | Accepted after revision 2025/10/09

HOW TO CITE: Zhang, F., Ma, F., Liu, W., Li, T., Li, S. (2025). An Efficient Algorithm for Distinguishing Triple Negative Breast Cancer with Ultrasound Image and High-dimensional Radiomics Data. *Information Technology and Control*, 54(4), 1459-1479. https://doi.org/10.5755/j01.itc.54.4.42585

An Efficient Algorithm for Distinguishing Triple Negative Breast Cancer with Ultrasound Image and High-dimensional Radiomics Data

Fen Zhang, Fucheng Ma

The 3rd Affiliated Teaching Hospital of Xinjiang Medical University (Affiliated Cancer Hospital), Urumqi, 830011, Xinjiang, China; e-mails: mary8479@163.com (F. Z.); mafuchengchao@sina.com (F. M.)

Wen Liu*

Artificial Intelligence and Smart Mine Engineering Technology Center, Xinjiang Institute of Engineering, Urumqi, 830023, China;

Xinjiang Changsen Data Technology Co., Ltd, Urumqi, 830063, China; e-mail: liuwen@xjie.edu.cn

Taojuan Li, Shanshan Li

School of Computer Science and Technology, Xinjiang Normal University, Ürümqi 830000, China;

e-mails: 2573601697@qq.com; 2006021@xjie.edu.cn (S. L.)

Corresponding author: liuwen@xjie.edu.cn

Triple negative breast cancer develops rapidly with high mortality and limited treatment. Therefore, it is important to detect and diagnose breast cancer in a timely manner. However, breast tumors in ultrasound images are characterized by irregular shapes, large-scale changes, and blurry boundaries, which bring great challenges to the segmentation and classification of breast ultrasound images. In this paper, we propose an approach for ultrasound image segmentation and classification of Triple Negative Breast Cancer (TNBC) and Non-Triple Negative Breast Cancer (NTNBC) based on deep learning and radiomics. Regarding the

deep learning framework, we propose a benign and malignant segmentation model based on the U-Net model for Channel and Spatial Efficient U-Net (CSE-U-Net) breast ultrasounds. First, during the skip connection stage, to obtain more spatial and contextual semantic information, we implemented a channel attention module (CM) and spatial awareness module (SM). Then, Efficient Channel Attention (ECA) is added to the feature extraction part of the U-Net backbone network to ensure model robustness. Regarding the radiomics, we extract features using histogram, texture, and filter features, and compare them using six machine learning classification algorithms. Experimental results indicate that CSE-U-Net is more effective and accurate in many evaluation indexes; among the six Machine Learning (ML) algorithms evaluated, the extreme gradient boosting algorithm was able to classify breast cancer more accurately into TNBC and NTNBC than the other five algorithms evaluated. The prediction results show that the CSE-U-Net and ML algorithms are efficient and can be used for the segmentation and classification of breast cancer into TNBC and NTNBC.

KEYWORDS: Breast ultrasound imaging; Deep learning; Radiomics; Machine learning

1. Introduction

1.1. Background and Significance

According to GLOBOCAN, the global cancer data for 2020 show that there are more than 226,000 ongoing breast cancer cases in women, ranking first in the world [31]. The high incidence age of breast cancer is between 45 and 54 [6]. However, the main cause of breast cancer remains unclear. Malignant tumors can be classified into TNBC and NTNBC based on their receptors. When the progesterone receptor (PR), human epidermal growth factor receptor 2 (HER-2), and estrogen receptor (ER) are all negative, the tumors are classified as TNBC; otherwise, they are classified as NTNBC [3]. Patients with TNBC exhibit low survival rates, poor prognoses, and rapid disease development. However, studies have confirmed that early detection and aggressive treatment can greatly improve patient survival and prognosis [4]. Histopathological detection is a traumatic operation; however, it is the gold standard for the diagnosis of breast cancer.

The probability of benign tumors being detected histopathological is approximately 70%, which causes physical and psychological trauma to patients with benign breast tumors. There are many ways to screen for breast cancer, among which breast ultrasound is non-invasive, real-time visualization, cheap, etc. It is regarded as one of the most effective routine breast screening methods [33]. Breast tumors in ultrasound images are of different sizes, have unclear boundaries, and are easily confused with other normal breast tissues [12]. Radiologists are often subjective in their diagnosis, and it is difficult to achieve an accurate diagnosis. Therefore, we first used an image segmentation algorithm to automatically distinguish between benign and malignant tumors and segment the tumor area and location. Then, we used radiomics approaches to extract features of TNBC and NTNBC from malignant tumors and machine learning algorithms for classification. The most meaningful thing is that we can predict the results of biopsy and immunohistochemistry in advance using only ultrasound images.

The rest of this section describes deep learning image segmentation technology and radiomics texture feature extraction and classification technology.

1.2. Related Research

With the widespread application of computer technology in breast ultrasound imaging, scholars have proposed various medical image segmentation algorithms. In the machine learning field, we are faced with challenges such as complex breast tissue structures, low contrast, speckle noise, and poor ultrasound imaging quality. Abdullah et al. [21] investigated the classification of breast tumors using handcrafted texture, shape, and intensity features extracted from ultrasound images, employing both Support Vector Machines (SVM) and Artificial Neural Networks (ANN). Their results demonstrated high specificity and balanced diagnostic accuracy, particularly in differentiating between benign and

malignant lesions. However, the dependence on manually engineered features may reduce generalizability across different imaging environments. To address this, Guizani et al. [13] proposed a hybrid CNN-SVM framework in which deep features were automatically extracted using convolutional neural networks (CNNs), such as MobileNetV2 and InceptionV3, and subsequently classified using SVMs. This two-stage pipeline leveraged both deep learning's representation power and traditional classifiers' robustness, achieving improved classification accuracy in breast cancer detection. Additionally, Ru et al. [26] introduced a hybrid spatial–geometric learning approach that combined CNNs with graph-based models to capture spatial relationships and geometric patterns in multi-center ultrasound datasets. Their approach outperformed traditional classification schemes, demonstrating excellent generalization and reliability for breast tumor differentiation.Despite these advances, conventional machine learning methods still require substantial manual intervention for feature engineering and parameter tuning, limiting their adaptability and scalability. Furthermore, their performance is often hindered by limited data availability and poor generalization across imaging conditions and clinical settings.

Currently, the primary deep learning algorithms for breast ultrasound image segmentation include U-Net [25], FCN [29], CSST-Net [44] and GAN-based methods [14]. Authors in [43] propose attention mechanisms to assist the network in concentrating on important regions. Among these, the U-Net architecture effectively combines low-level (shallow) and high-level (deep) image features, achieving accurate segmentation even with limited training data, which makes it particularly suitable for medical imaging tasks. To tackle the challenge of segmenting complex tumor boundaries in breast ultrasound images, Wan et al. [34] proposed a dual-path D-TransUNet model that integrates convolutional neural networks (CNNs) and transformers. The CNN path captures local texture details, while the transformer path models global dependencies, resulting in enhanced edge sensitivity and more precise delineation of irregular tumor contours, especially under low-contrast conditions. Anand et al. [2] reformulated breast ultrasound segmentation as a mask classification problem using the Mask-Former architecture. Leveraging cross-spatial attention mechanisms, their model effectively aggregates contextual information, producing coherent and accurate segmentations across diverse tumor types. This approach achieved state-of-the-art results on several public datasets. Rao et al. [23] developed an ensemble transfer learning framework for breast ultrasound diagnosis by stacking pretrained CNN feature extractors—including InceptionV3 and VGG-16/19—and combining classifiers such as Multi-Layer Perceptron (MLP) and Support Vector Machines (SVM). Their method demonstrated improved robustness compared to standard CNNs, achieving an AUC of 0.947 and an accuracy of 0.858.

Although many scholars have proposed different segmentation methods for breast tumor ultrasound images, there remain unresolved problems. First, there is an overlap in the benign and malignant manifestations of breast ultrasound images, which is prone to misjudgment, and using only the information acquired from breast images to judge benign and malignant is too biased. Second, most researchers only classify benign and malignant breast cancers and have not studied the crucial TNBC and NTNBC classifications. Therefore, we introduced a radiomics method to evaluate TNBC and NTNBC in malignant tumors based on segmentation results.

Radiomics, since its introduction by Lambin et al. [18], has been widely applied in breast cancer diagnosis and prognosis evaluation. Recent advances integrating ultrasound radiomics and machine learning have demonstrated significant progress in classifying and predicting outcomes for triple-negative breast cancer (TNBC). Wenwen et al. [36] conducted a multicenter study developing a machine learning model that combined ultrasound radiomic features with clinicopathological data to predict disease-free survival (DFS) in patients with non-metastatic TNBC. Their model demonstrated strong prognostic performance, achieving AUCs of 0.84 in the training cohort and 0.90 in the external validation cohort. Li and Duan [19] retrospectively analyzed data from 127 breast tumor patients and evaluated four machine learning algorithms—logistic regression, support vector machine, decision tree, and random forest—to build predictive models for TNBC. The integrated model achieved AUCs of 0.92 and 0.76 in the training and test sets, respectively,

outperforming models based on single feature types. In a related study, Cai et al. [8] explored the use of ultrasound radiomics to identify TNBC in a retrospective single-center cohort. Their findings confirmed that radiomic features derived from B-mode ultrasound images could effectively distinguish TNBC from non-TNBC subtypes, highlighting the important diagnostic value of texture-based radiomic features. Collectively, these studies underscore the growing utility of radiomics combined with machine learning in improving the diagnosis, risk stratification, and treatment planning of TNBC.

Considering the ultrasound images for breast tumors with different sizes, low contrast, unclear demarcation between tumor and normal tissue, etc. we propose a Channel and Spatial Efficient U-Net (CSE-U-Net) breast ultrasound image segmentation model based on deep learning. First, CM and SM were introduced in the jump connection phase of the U-Net model to extract the breast ultrasound image edge information. Then, to improve the model performance without increasing its complexity, we added the ECA (Efficient Channel Attention) spatial attention mechanism to the main feature extraction network to distinguish between benign and malignant breast ultrasound images. To perform a qualitative analysis of malignant TNBC and NTNBC tumors after breast ultrasound segmentation, we used radiomics techniques, such as histogram features, texture features, and filter features, to extract image features from multiple angles, and built models using multiple machine learning algorithms. The experimental results show that the proposed breast ultrasound segmentation model has a better segmentation result than that of the original model. Furthermore, the random forest and XGB algorithms perform the best in extracting TNBC and NTNBC tumor features.

The remainder of this paper is organized as follows. Section 2 introduces the image segmentation methods for breast ultrasound image tumors and feature extraction methods for TNBC and NTNBC images based on radiomics. Section 3 introduces the experimental validation and analysis of the methods proposed in Section 2 using breast ultrasound image datasets and public datasets of the tumor hospital affiliated with Xinjiang Medical University. Finally, Section 4 summarizes the entire study.

2. Image Segmentation and Radiomics

2.1. Image Segmentation

Malignant and benign tumors in breast ultrasound images usually have different features. Benign tumors are smooth with clear or sharp edges, oval, and large lobulated. Malignant tumors are not smooth, have blurry edges, and are small, lobulated, and spiculated. The boundary features of tumors can not only help improve the accuracy of imaging, helping doctors in differentiating benign and malignant tumors, but also are crucial in the segmentation and classification of breast ultrasound images. Currently, with the development of artificial intelligence technology, deep learning technology is increasingly being used in medical imagery. Many scholars have proposed various medical image-segmentation technologies [10]. The U-Net algorithm is currently one of the most widely used algorithms for medical image segmentation. First, the algorithm uses an encoder backbone feature network to extract features from the image to obtain five effective feature layers. Second, it uses a decoder to enhance the features and fuse the effective feature layers to obtain a feature layer that integrates all obtained features. Then, it uses the last feature layer to predict each pixel. Inspired by the literature, we used the U-Net model as the benchmark model for breast ultrasound images. After semantic segmentation of breast ultrasound images, it is necessary to classify the feature maps. Acquiring breast tumor features can pave the way for accurate tumor diagnosis.

2.1.1. Network Architecture

To better segment the shape and edge of breast ultrasound images, we propose the so-called CSE-U-Net model, CSE represents CM, SM and ECA modules respectively. CSE represents CM, SM and ECA modules where principles of CM and SM are explained in section 2.1.2 and principles of ECA are explained in section 2.1.3. The CSE-U-Net structure of which is shown in Figure 1.

The CSE-U-Net model is divided into image data preprocessing, image deep learning, and image prediction stages. (1) Image data preprocessing stage aims to reduce model overfitting, weaken data noise,

Figure 1

CSE-U-Net network architecture. Sections 2.1.2 and 2.1.3 describe the CM, SM, and ECA attention.

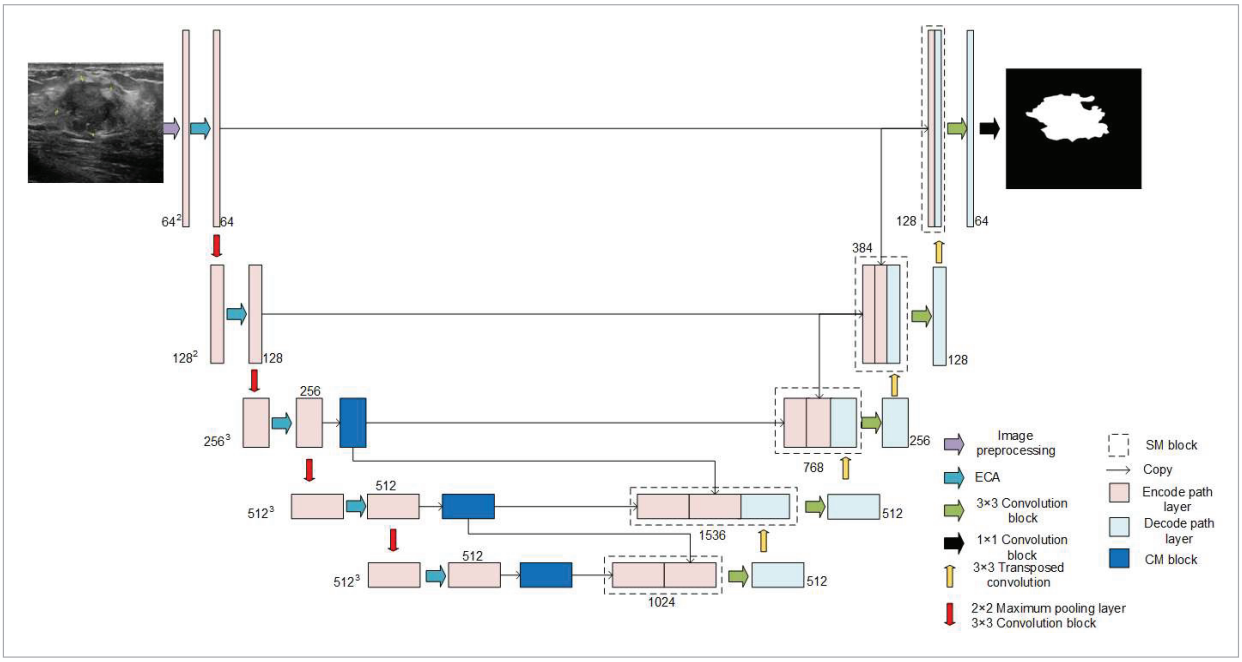

and enhance the generalization of the model. First, the model performs random horizontal flipping, skewing, and Gaussian blurring operations on the input image in this stage to increase the number of data samples. Second, normalization and regularization are applied. Finally, the image is uniformly cropped to 512 pixels × 512 pixels. (2) The learning stage mainly comprises an encoder, decoder, ECA, CM, and SM. For better end-to-end semantic segmentation, the encoder and decoder structures refer to the overall structure of U-Net symmetry. In the encoder stage, also known as the down-sampling stage, the main purpose is to extract the tumor features in breast ultrasound images. This stage is divided into five layers, mainly composed of several 3 × 3 convolution blocks (3 × 3 convolution layer, batch normal, and ReLU activation function), a 2 × 2 average pooling layer, an ECA, and an attention mechanism. The purpose of the convolution block is to obtain image features and improve the expression ability regarding the nonlinear model features. Therefore, each feature layer needs to perform 3 × 3 convolution block operations, in which the first two layers need to be operated twice and the last three layers need to be operated three times. For every execution of the 2 × 2 average pooling layers, the space size of the feature layer is reduced once, and the number of channels is unchanged. This module reduces the feature dimension and overfitting and enhances the model fault tolerance. The ECA attention mechanism effectively extracts dependencies between channels without increasing the number of parameters. In the decoder stage, also known as the up-sampling stage, the purpose is to enhance the resolution and feature information of the image, mainly including several feature fusions, SM module, 3 × 3 transposed convolution, and 3 × 3 convolution block composition. Shallow convolution can obtain better texture features, whereas deep convolution focuses more on the essential features of the image. The traditional U-Net network fuses only the weighted features of the corresponding feature layers, which results in a loss of spatial and semantic feature information. Therefore, the SM module was used in the jump connection stage to extract more semantic information and fuse it with the feature layer in the up-sampling stage. The decoder successively enhances the feature extraction performance of the feature layer that integrates all semantic information and gradually recovers the image information, making the net-

work more accurate and stable. (3) Image prediction stage, using 1 × 1 convolution blocks, predicts each pixel category of the image.

2.1.2. Channel and Spatial Modules

In ultrasound images, most tumors are hypoechoic, and the quality of tumor images is closely related to the medical methods. As reported by Ibtehaz et al. [16], ultrasound images of breast tumors have different shapes and sizes, unclear textures, and unclear boundaries between the tumor and the normal breast tissue. In this study, we propose a CM module for multi-scale extraction of context channel information and an SM module for spatial information. First, we replace the single-scale convolution with multi-branch convolution to obtain different scale perception fields and stitch and fuse features of different scales to enhance the context feature extraction ability. On the other hand, to recover the spatial information lost in the down-sampling during the U-Net skip connection stage, we fused the shallow features with the deep features and replaced the original intermediate features to weaken the feature differences in the coding and decoding processes.

The structure of the CM module is illustrated in Figure 2. First, feature map I was passed through one 1 × 1 convolution and three 3 × 3 convolution branches. The 3 × 3 convolution branches enlarge the receptive field by increasing the number of convolution cores, replacing large convolution cores, reducing the computational complexity, and improving the model detection speed. The number of convolution cores in the three branches was 1, 2, and 3. Then, four convolution branches from different receptive fields are fused to obtain the feature map K. To fully leverage the contextual semantic information, we introduce a refined attention mechanism (ARM) [38] that captures feature weight information at different scales to obtain feature map P without increasing computational costs. The ARM includes global average pooling, 1 × 1 Convolution, Batch Normal, and Sigmoid operations.

Figure 2
CM module architecture.

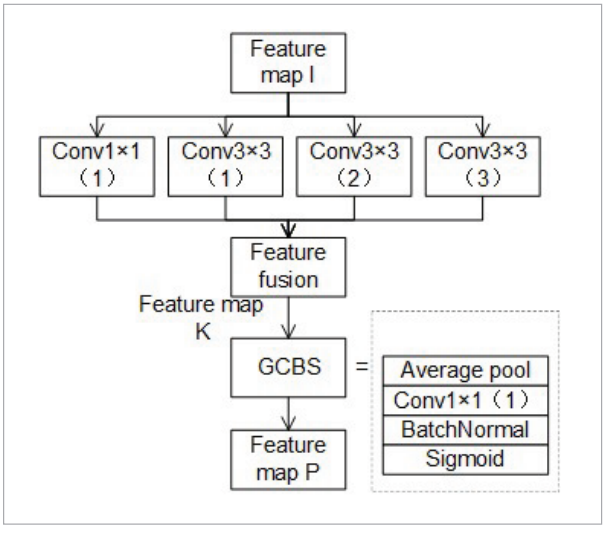

In the U-Net network, the down-sampling process compresses the image information. Subsequently, directly using up-sampling to recover the image will cause losing significant feature information. Therefore, a skip connection is introduced to provide multi-scale spatial information for the up-sampling deconvolution stage, which makes the segmentation finer. However, skip joining has some limitations. Fusing the shallow information obtained from down-sampling directly with the deep information obtained from up-sampling will result in differences in semantic information and loss of fine-grained information, such as edge and texture information of tumors. Accordingly, we proposed an SM module for extracting multi-scale spatial information fusion. The structure of the SM module is illustrated in Figure 3. The feature layer fusion part must aggregate the multi-scale spatial and channel information of the adjacent feature layers. For example, for the feature fusion operation in the i layer, the $C_{i-1,j}$ feature layer of the i-1 layer must be divided into four parts in the encoder. First, the $C_{i-1,j+1}$ and $C_{i,j+1}$ feature layers are obtained by the CM module and 3×3 convolution block. Second, the $C_{i-1,j}$ feature layer is average pooled to obtain $C_{i,j}$ feature layers. Then, in the decoder part, layer $C_{i+1,j}$ is used for 3×3 transposition convolution operations to obtain $C_{i,j+2}$ feature layers. Finally, $C_{i,j}$ feature layers, $C_{i,j+1}$ feature layers, and $C_{i,j+2}$ feature layers are fused with weighted features and 3×3 convolution blocks to obtain $C_{i,j+3}$ feature layers. The MS module is defined as stated in Equation (1).

$$C_{i,j+3}=F\left(A\left(C_{i-1,j}\right)+C\left(C_{i-1,j+1}\right)+T\left(C_{i+1,j}\right)\right) \quad (1<i<5) \tag{1}$$

Figure 3
SM module architecture.

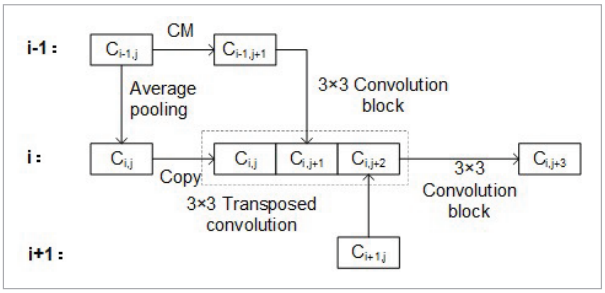

Here, F denotes the feature fusion operation, A denotes the average pooling operation, the step size is 2, the size of the feature layer becomes half of the original, and the number of channels remains unchanged. C denotes the convolution block operation, which includes a 3×3 convolution kernel, Batch Normal and ReLU activation functions, and T-transpose convolution converts low resolution to high resolution.

2.1.3. ECA Attention Mechanism

Many feature layers were captured during the down-sampling process. To further determine the importance of each channel in the feature layer, different weights are assigned according to channel importance so that more attention is paid to the important features, and less important channel features are suppressed during model learning. To further determine the importance of each channel in the feature layer, different weights are assigned based on the channel importance so that the model pays more attention to the important features and suppresses the unimportant channel features when learning. To address this problem, Jie et al. [15] proposed an SENet attention mechanism. However, Wang et al. [35] believed that although the SENet network improved the performance of the model, it increased the model complexity when reducing dimensions. Therefore, they proposed an attention mechanism module of efficient channel attention (ECA). The ECA attention mechanism not only avoids dimension reduction but also enables cross-channel feature information interaction. The structure of the ECA network is illustrated in Figure 4. The module includes the following four steps:

Figure 4
ECA attention mechanism.

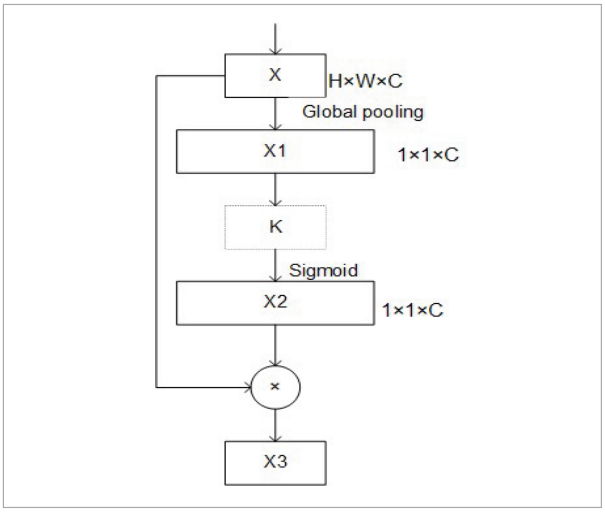

First, the input feature map X(H×W×C) is defined, and X1(1×1×C) is obtained via global average pooling, as stated in equations (2) and (3), where K (2-D convolution, both length and width of convolution core are K) is the convolution kernel size and S is the step size.

$$W=\frac{W-K}{S}+1 \tag{2}$$

$$H=\frac{H-K}{S}+1. \tag{3}$$

Second, the adaptive convolution kernel K is calculated according to the channel number C of the X1 characteristic diagram, as stated in formula (4), where "|t|odd" represents the odd number of the nearest t:

$$K=\left|\frac{\log_2(C)}{2}+\frac{1}{2}\right|\text{odd}. \tag{4}$$

Then, the feature map X1 calculates the feature weight of each channel through the convolution kernel K and then uses the Sigmoid function to assign weight to each feature channel to obtain the feature map X2, as stated in equation (5), where y_i represents a feature layer.

$$W=\text{Sigmoid}\left(C(y_i)\right)\ \ i\in C. \tag{5}$$

Finally, X2 and X are multiplied channel-by-channel to generate a weighted feature map X3.

2.2. Radiomics

TNBC and NTNBC breast cancers have similar sonographic findings and overlapping lesion features. However, Radiomics can be automated during the

deep mining and analysis of the heterogeneity of breast tumors. Combining imaging and tumor features can provide useful information for clinical diagnosis. The main processes of radiomics include image pre-processing, image feature extraction, model establishment, and verification, as shown in Figure 5.

Firstly, the tumor captured in the breast ultrasound image is semantically segmented to extract its focus area, and then its image features are extracted. The feature extraction [28] mainly includes histogram, texture, and filter features. Histogram features are representations of pixel intensity that do not change with scale, shift, and rotation. We focus on first order features, which amounts to a total of 18 features. Texture feature [22] refers to the quantification of image features. The main extraction methods are structure-based and statistics-based methods, which have good anti-jamming ability against noise and rotation invariance. We use the 16-feature Gray-Level Size Zone Matrix (GLSZM), 5-feature Neighboring Gray Tone Difference Matrix (NGTDM), 24-feature Gray-Level Co-occurrence Matrix (GLCM), 16-feature Gray-Level Run-Length Matrix (GLRLM), and 14-feature Gray-Level Dependence Matrix (GLDM). Filtering feature [27] is an indispensable part of the image preprocessing stage. It can preserve the original image information while reducing the noise inter-ference. In this study, we select the wavelet transform for feature extraction. Python's wavelet filter (which has 48 wavelet bases) can process the images. Each wavelet base has eight different filtering methods for image filtering in low-pass and high-pass modes. Each filtering method uses 14 first-order statistics. Each image will generate 5376 (48*8*14) features. If various filters and classification features are combined, each image can extract more features. For instance, if the above methods are combined with 63 texture-based features, the image will extract 48*8*(14+63) = 29568 features.

The feature dimensions of the medical images were higher than those of the nor-mal images. In this study, we used radiomics to extract features of

Figure 5
Radiomics flowchart.

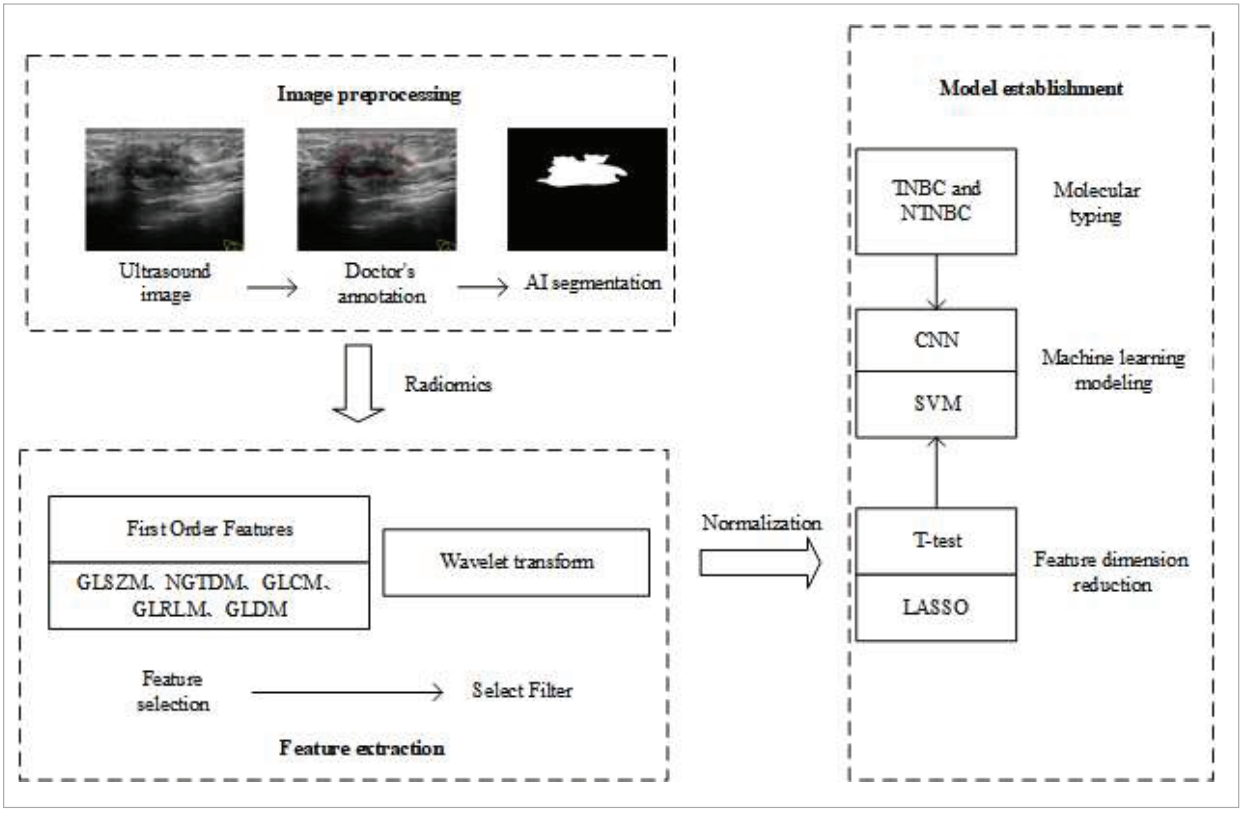

TNBC and NTNBC. In total, 465 features were extracted in this study. Among these, there are many redundant features; many features for model training will lead to over-fitting; therefore, before model training, we used Student's t test and Least Absolute Shrinkage and Se-lection Operator (LASSO) [37] to reduce duplicate variables and filter the most important features for model training. we used LASSO to achieve feature selection and dimensionality reduction of high-dimensional radiomics data. Lasso is a method in statistical learning used to solve variable selection and regularization in linear regression problems. LASSO achieves feature selection and dimensionality reduction by adding L1 regularization terms to the loss function to make the coefficients of some features zero. Finally, this study uses a machine learning algorithm to model the TNBC and NTNBC features and employs a 10-fold cross-validation method to train the model and evaluate the classifier performance.

2.2.1. Normalization

Data normalization is a common data preprocessing process that can eliminate data singularities, accelerate the model convergence speed, and improve the model classification accuracy. We used the z-score [40] to compress the data, as stated in equation 6:

$$Z=\frac{x-\mu}{\sigma}, \tag{6}$$

where x, μ, and σ are the pixel value, average pixel value, and average pixel standard deviation, respectively.

2.2.2. Feature Dimension Reduction

High-dimensional data indicate that the data dimensions are far greater than the number of samples. If we directly use high-dimensional data for model training, it will lead to over-fitting of the model, which will be difficult to predict. Data dimensionality reduction is an indispensable part of selecting important features. There are two main steps to reduce the dimension of data features: first, a paired sample Student's t test is used to detect whether the mean of the data are equal to each other, so that the two samples are independent and obey the normal distribution. Second, the penalty function of the LASSO method was used to reduce the variable set and compress the coefficient to zero. This method has a wide range of applications, which can not only filter variables but also reduce the complexity of the model to avoid overfitting.

The Student's t test is divided into single-sample Student's t test, paired-sample Student's t test and independent-sample Student's t test according to the applicable scenarios of the samples. The samples studied in this paper are suitable for independent-sample Student's t test, and the implementation principle is as follows.

Step 1: Assume assumptions. H0 (No significant difference between the two samples), H1 (Significant difference between the two samples).

Step 2: Decision strategy (α=0.05).

Step 3: Calculate the t-score, as shown in equation (7) - (8).

$$t=\frac{\bar{x}-\bar{y}}{S_w\sqrt{\frac{1}{m}+\frac{1}{n}}}\sim t(m+n-2) \tag{7}$$

$$S_w=\frac{1}{m+n+1}\left[(m-1)S_1^2+(n-1)S_2^2\right]. \tag{8}$$

Equations (7)-(8), in which $\bar{x}$, m, S_1^2, represents the mean, capacity and variance of the first sample, $\bar{y}$, n, S_2^2 represent the mean, capacity and variance of the second sample, respectively.

Step 4: Make judgments and conclude with H_0.

The core principle of LASSO method is to change the unimportant characteristic coefficient to 0. The realization principle is as follows:

Step 1: Define the model function as shown in Formula (9):

$$y_i=w_i^T x_i+b, \tag{9}$$

Formula (9) y_i represents the predicted value, X_i represents the characteristic value and w_i represents the weight value of the characteristic.

Step 2: Learn the weight w and the cost objective function is shown in Formula (10).

$$J(w)=\frac{1}{m}\sum_{i=1}^{m}\left(y_i-w^T x_i\right)^2+\lambda\sum_{i=1}^{m}|w_i|. \tag{10}$$

Formula (10) λ(Lambda)>0, m represents the number of features, the smaller the cost loss function, the more accurate the forecast value will be, so both $\sum_{i=1}^{m}(y_i-w^T x_i)^2$ and $\lambda\sum_{i=1}^{m}|w_i|$ need to be as small as

possible. The larger the λ value, the more weight coefficients will be compressed, and many coefficients will be compressed to 0. The value of λ will be verified by cross-validation with ten folds.

Step 3: L1 regularization is used to compress the dimension of characteristic data and the approximate gradient descent method [39] is used to iteratively solve the optimal W value.

In this paper, we used radiomics to extract 465 features from breast ultrasound images, and then Student's t test and Lasso method were used for calculation and analysis. 8 important features were obtained, which have obvious classification significance at the statistical level.

This chapter mainly introduced the network model of CSE-U-Net and the method to extract the features from the image group. Next, the experiments and analysis of the method would be carried out to verify its accuracy and accuracy.

3. Datasets and Experimental Analysis

3.1. Datasets

Image Segmentation: (1) Public datasets: Breast Ultrasound Images Dataset (Dataset BUSI) [1]: The dataset collected ultrasound breast images of women aged between 20 and 75 years, including 133 normal images, 437 benign images, and 210 malignant lesions, with an average pixel value of 500×500; the dataset is masked by manual labeling. (2) Breast Ultrasound Image Datasets (XJBUSI) of Affiliated Tumor Hospital of Xinjiang Medical University: The dataset was acquired using a Logic-E9 color Doppler ultrasound system with an image frequency range of 5–9 MHz and mechanical index of 0.16. The images show the morphology, lesions, and surrounding tissues of the patient's breast tumors. The selected dataset consisted of 920 malignant and 400 benign lesions, with an average pixel value of 1008×547. The dataset tumor regions were labeled using the labelme tool and examined by two physicians with five years of clinical experience.

Radiomics: In this study, 300 patients with TNBC and NTNBC, confirmed by surgery and pathology, were enrolled in the Affiliated Tumor Hospital of Xinjiang Medical University between January 2015 and December 2012. Among them, 150 were classified as having TNBC and 150 as having NTNBC. The inclusion criteria were as follows: (1) All patients underwent ultrasonography before surgery, and complete ultrasonographic data were retained. (2) All patients were confirmed by pathological results. Exclusion criteria were as follows: (1) No definite pathological results were found in patients who were not treated with hospital-type surgery for cancer. (2) The information regarding retained ultrasound images was incomplete with poor quality. Examples of TNBC and NTNBC are presented in Figure 6.

Figure 6
Example diagrams of TNBC and NTNBC.

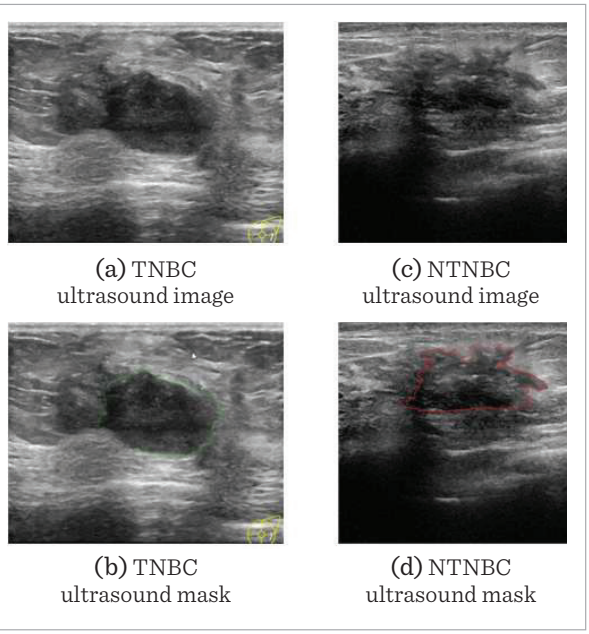

3.2. Evaluation Index

To evaluate and test the performance and advantages of the CSE-U-Net model, we used the Precision (P), Recall (R), Accuracy (Acc), Mean Intersection over union (MIou), and Frequency-Weighted Intersection-over-union (FWIou) metrics as evaluation indexes. P refers to the correct proportion of positive sample prediction in the prediction results, R refers to the proportion of positive samples predicted to be correct, Acc re-fers to the proportion of positive samples and negative samples predicted correctly in

the prediction, MIou refers to the ratio of union and intersection of each type of real value and predicted value, and FWIou is an improvement of the MIou evaluation indicators, which sets weights for the frequency of each category.

Equations (11)–(15) are stated as follows:

$$\text{Precision}=\frac{TP}{TP+FP} \tag{11}$$

$$\text{Recall}=\frac{TP}{TP+FN} \tag{12}$$

$$\text{Accuracy}=\frac{TP+TN}{TP+FP+TN+FN} \tag{13}$$

$$\text{MIou}=\frac{1}{k+1}\sum_{i=0}^{k}\frac{TP}{FN+FP+TP} \tag{14}$$

$$\text{FWIou}=\frac{TP+FN}{TP+FP+TN+FN}\times\frac{TP}{TP+FP+FN}, \tag{15}$$

where True Positive (TP) denotes the number of positive samples predicted correctly, False Positive (FP) denotes the number of positive samples predicted as negative samples, True Negative (TN) denotes the number of negative samples predicted correctly, and False Negative (FN) denotes the number of negative samples predicted as positive samples. As the essence of image segmentation is the classification of pixel categories, K represents the number of pixel categories.

The Mean Square Error (MSE), accuracy, sensitivity and specificity are often used in radiomics to measure the effectiveness of medical image classification. The MSE is the expected value of the square of the difference between the true and predicted values. The smaller the MSE is, the better is the model accuracy, as stated in Equation (16), where y_i represents the true value, $\hat{y}_i$ represents the predicted value, and m represents the number of samples. The accuracy was calculated using Equation (13). Sensitivity is also known as the recall rate, as stated in equation (12). Specificity refers to the ratio of the correct negative samples to the total negative samples, as stated in Equation (17). The F1-Score is the harmonic average of P and R, as stated in equation (18). The ROC curve, whose area is the value of Area Under Curve (AUC), measures the generalization performance of the model.

$$\text{MSE}=\frac{1}{m}\sum_{i=1}^{m}\left(y_i-\hat{y}_i\right) \tag{16}$$

$$\text{Specificity}=\frac{TN}{TN+FP} \tag{17}$$

$$F_1=2\times\frac{P\times R}{P+R}. \tag{18}$$

3.3. Experimental Environment

The operating system of the experimental environment was Windows 11, CPU was Intel Xeon E5 V3 2600, memory size was 16G, GPU model was NVIDIA RTX3090 with CUDA version 11.4, memory size was 24G, and deep learning framework was Pytorch 1.9.0.

We use SGD optimizer, Adam optimizer, RMSprop optimizer and Adagrad optimizer to adjust the parameters of the deep learning algorithm, and finally test that the SGD optimizer has achieved the best results. The initial learning rate is adjusted from 0.1 to 0.01, each time reduced by 0.01, and the final initial learning rate is determined to be 0.05; Batchsize uses the maximum within the GPU limit; After testing, when epoch is greater than 180, the model tends to converge. Therefore, epoch 200 is set in this paper to ensure the convergence of the model while reducing the time waste. The momentum is 0.99 to 0.01 and the final value is determined by grid search. Weighted at-tenuation coefficient using default value 0.0001. Lasso Alpha = λ in radiomics experiments, taking 50 values from the linearity in - 4 and 1, Lasso max_iter was set to 100000, and cross validated parameters were set, using a mean square error assessment, resulting in an optimal value for lasso modeling; Optimization of relevant hyperparameters in machine learning classification methods using grid search methods such as the Number of Weak Optimizers in extreme gradient boosting (XGB) [9] set to 200, Random Forest (RF) [7] Random_state was set to 20, information gain was selected by Feature method in Support Vector Machine (SVM) [30] and kernel function was Radial Basis Function.

Parameter tuning in deep learning is an important step in the model training process, which directly affects performance, convergence speed, and generalization ability. The following is a detailed explanation and adjustment method for the main hyperparameters such as learning rate, epochs, and batch

size. The main parameter setting methods are summarized as follows:

Adjustment method for learning rate: Usually, we use random sampling on a logarithmic scale to select the learning rate, that is, sampling multiple times in the interval close to 0, because the learning rate is usually very sensitive in this interval.

Adjustment method for Number of iterations (Epochs): We determine the number of iterations based on the model convergence. Usually, we determine whether a model has converged by observing the loss or accuracy on the validation set. If the loss of the model does not significantly decrease or the accuracy does not improve after several consecutive iterations, the iteration can be stopped.

Adjustment method for Batch Size: The selection of batch size will affect the training speed of the model and the stability of gradient updates. We generally consider parameter values based on dataset size, model architecture, hardware resources, and training objectives, combined with empirical values.

The experimental parameters are listed in Table 1.

Table 1
Super-parametric settings.

Deep Learning		Radiomics	
Optimizer	SGD	Lasso Alpha	-4,1,50
Initial learning rate	0.05	Lasso max_iter	100000
Batch-size	4	Number of Weak Optimizers	200
epoch	200	Random_state	20
momentum	0.9	Feature method	information gain
Weight decay factor	0.0001	kernel function	Radial Basis Function

3.4. Experimental Results and Analysis

3.4.1. Experimental Results and Analysis of Image Segmentation

The samples in BUSI and XJBUSI datasets were randomly divided into a training set: verification set: test set=7:2:1; accordingly, experiments were conducted. The training set was used to train the model and adjust its parameters, verification set was used to find the optimal model, and test set was used to test the generalization of the trained model. To verify the effectiveness of the multiclassification CSE-U-Net model proposed in this study, we used ablation experiments to verify the effectiveness of adding CM, SM modules, and ECA attention mechanisms. The ablation experiment was based on the U-Net model. To make the model fuse the semantic information between multi-scale context channels, CM module was introduced in the third, fourth and fifth layers of the down-sampling stage, which was named U-Net+CM. To make the U-Net model use more spatial information and reduce the gap between the shal-low information and the deep information semantics of the model, an SM module named U-Net+SM was added throughout the jump connection stage. To further extract semantic information across channels, an ECA attention mechanism model named U-Net+ECA was added after each feature layer in the downsampling encoding phase. In addition, CM module is combined with ECA module, SM with ECA module, CM with SM module, CM, SM with ECA module. The models are named U-Net+CM+ECA, U-Net+SM+ECA, U-Net+CM+SM, CSE-U-Net respectively. Figures 7-8 show the results of ablation experiments on XJBUSI and BUSI Dataset datasets, respectively.

As shown in Figures 7-8, (1) U-Net+CM model: Acc and MIou reach 98.53%, 97.29% in XJBUSI dataset, 97.52% and 95.28% in BUSI dataset, respectively, which are 0.3%, 0.48%, 0.2%, 0.33% higher than the U-Net model, and its segmentation effect is better than that of the U-Net model. (2) U-Net+SM model: Acc and MIou reach 98.33%, 97.39% in XJBUSI dataset, 97.47%, 95.44% in BUSI dataset, 0.1%, 0.58%, 0.12%, 0.49% higher than the U-Net model, which improves the segmentation accuracy of the U-Net model; (3) U-Net+ECA model: Acc and MIou reach 98.53%, 97.39% in XJBUSI dataset, 97.33% and 95.07% in BUSI dataset, respectively, which are 0.3%, 0.04%, 0.52%, 0.12% higher than the U-Net model. This model has higher segmentation accuracy than the U-Net model. (4) The combined models U-Net + CM + ECA, U-Net + SM + ECA, U-Net + CM + SM, and CSE-U-Net compared with the addition of a single module enhanced the segmentation effect to various degrees, among which the CSE-U-Net model achieved the best segmentation effect.

Figure 7
Ablation results on XJBUSI dataset.

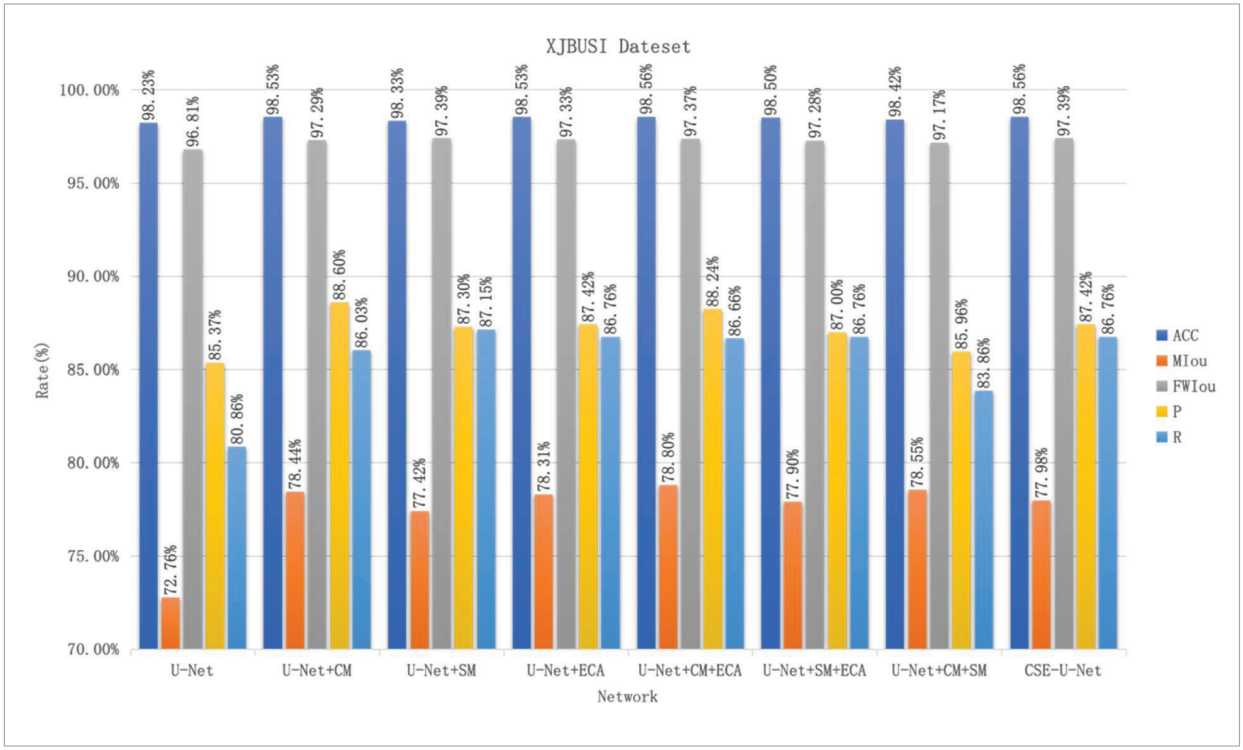

Figure 8
Ablation results on the BUSI dataset.

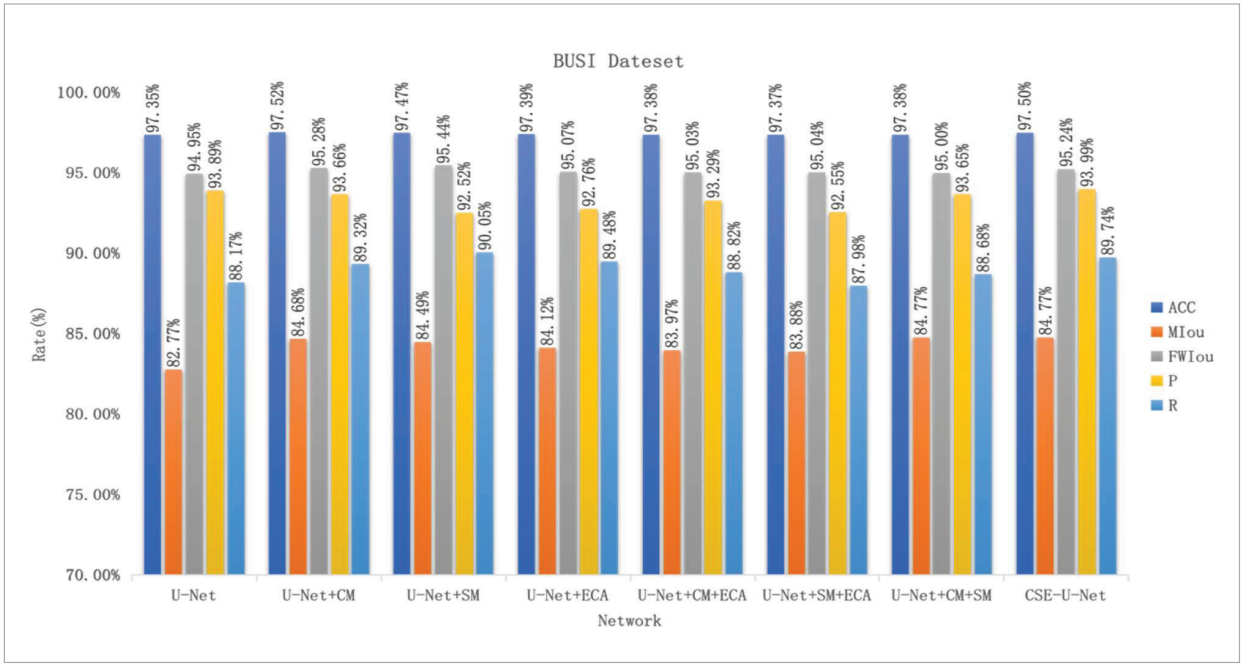

As shown in Figure 9, as an example plot of Ablation Experiment segmentation results, The CSE-U-Net model has better segmentation performance. SM and CM modules are added to the CSE-U-Net model to enhance the edge detection ability, and ECA attention mechanism is introduced to enhance the network feature extraction ability without increasing the computational load. The effect of texture blurring on the model detection is reduced. The CSE-U-Net model is significantly better than the original U-Net model for edge detection. The U-Net+CM+SM model has the same edge smoothness as the CSE-U-Net model. However, the detection accuracy is slightly lower than that of the CSE-U-Net model due to its weaker ability to extract image features.

As reported in Table 2, because the CM and SM modules increase the number of model parameters, the computational complexity of the model increases; accordingly, the detection speed of the model decreases. Because the ECA attention mechanism only adds a few parameters, it does not reduce the calculation speed of the model while improving the model accuracy. Compared with the other two models, CSE-U-Net improved in five indicators, indicating the generalization and effectiveness of the proposed algorithm.

In this study, we verify the segmentation performance of the proposed CSE-U-Net model. Using the same experimental environment and dataset, U-Net, AttNet [20], ERFNet [24], PSPNet [41], SegNet [5], and UNet++ [42] were compared with the CSE-U-Net model, as reported in Figures 10-11.

Figure 10 presents the evaluation index results of the different algorithms on the XJBUSI dataset. Compared with the other algorithms, the CSE-U-Net algorithm achieved the best results in five evaluation indexes. Compared with the best segmentation algorithm of the same kind, namely, PSPNet, in the comparison experiment, the proposed algorithm improved the Acc, MIou, FWIou, P, and R by at least 0.17%, 2.27%, 0.31%, 0.72%, and 2.95%, respectively. PSPNet is mainly used for the scene analysis of similar color and shape problems in im-

Table 2

Ablation results of FPS on XJBUSI and BUSI dataset.

Dataset	U-Net	U-Net +CM	U-Net +SM	U-Net +ECA	U-Net +CM+ECA	U-Net +SM+ECA	U-Net +CM+SM	CSE-U-Net
XJBUSI	0.1461s	0.1777s	0.1726s	0.1551s	0.1798s	0.1775s	0.1789s	0.1805s
BUSI	0.1022s	0.1376s	0.1334s	0.1175s	0.1382s	0.1371s	0.1383s	0.1392s

Figure 9

Example of the ablation experiment.

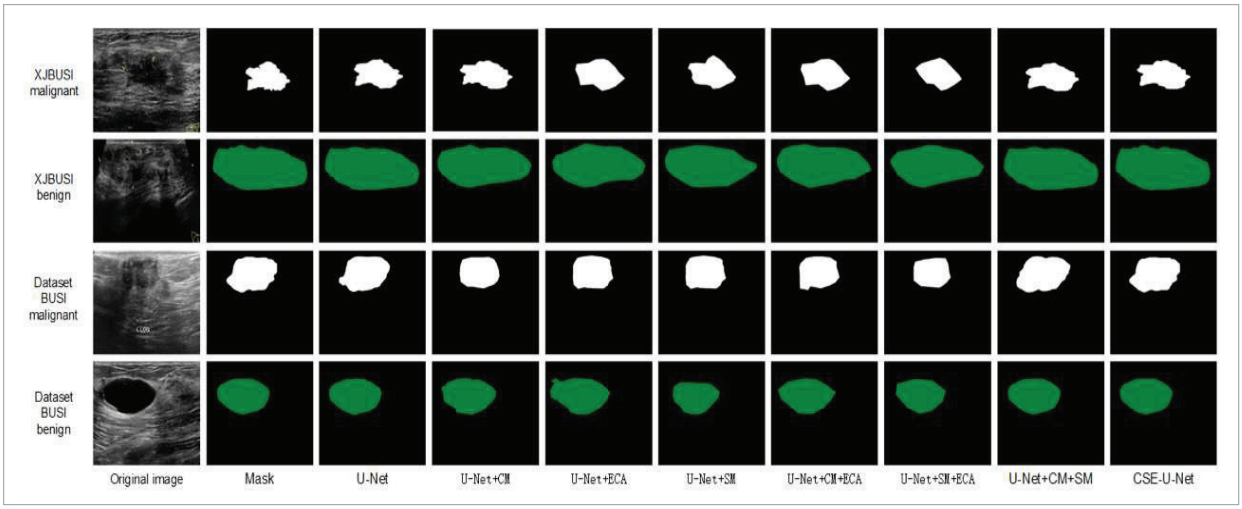

Figure 10
XJBUSI dataset performance comparison.

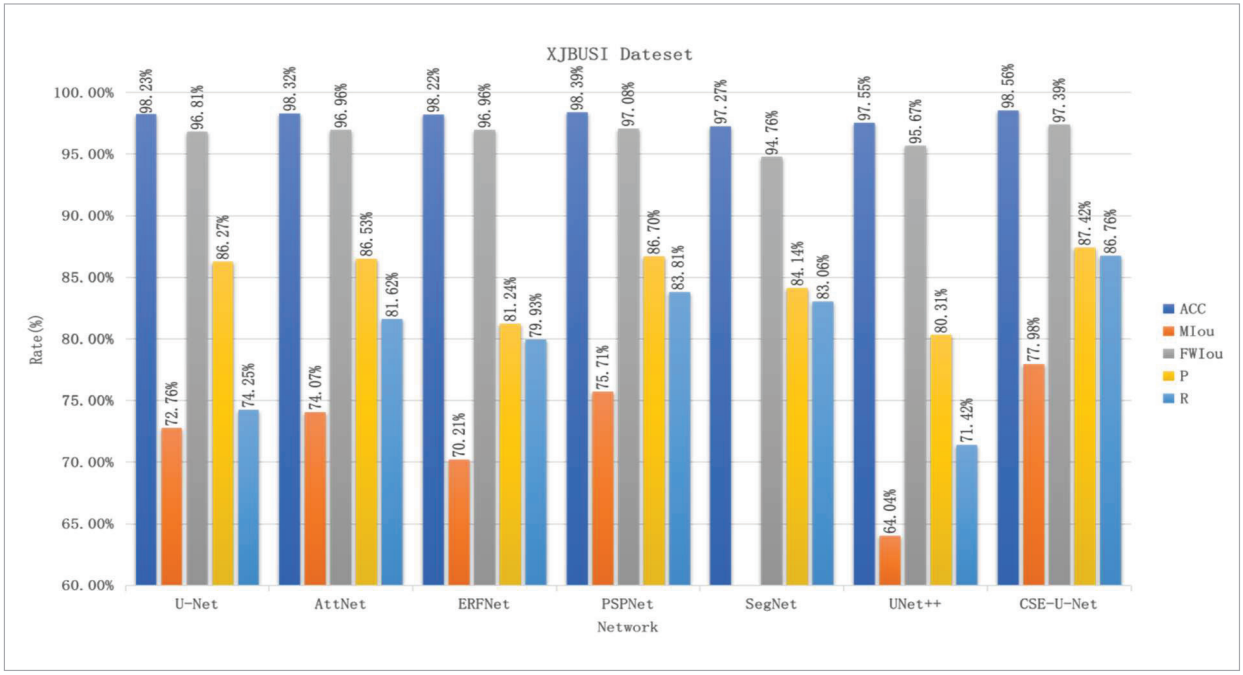

Figure 11
BUSI dataset performance comparison.

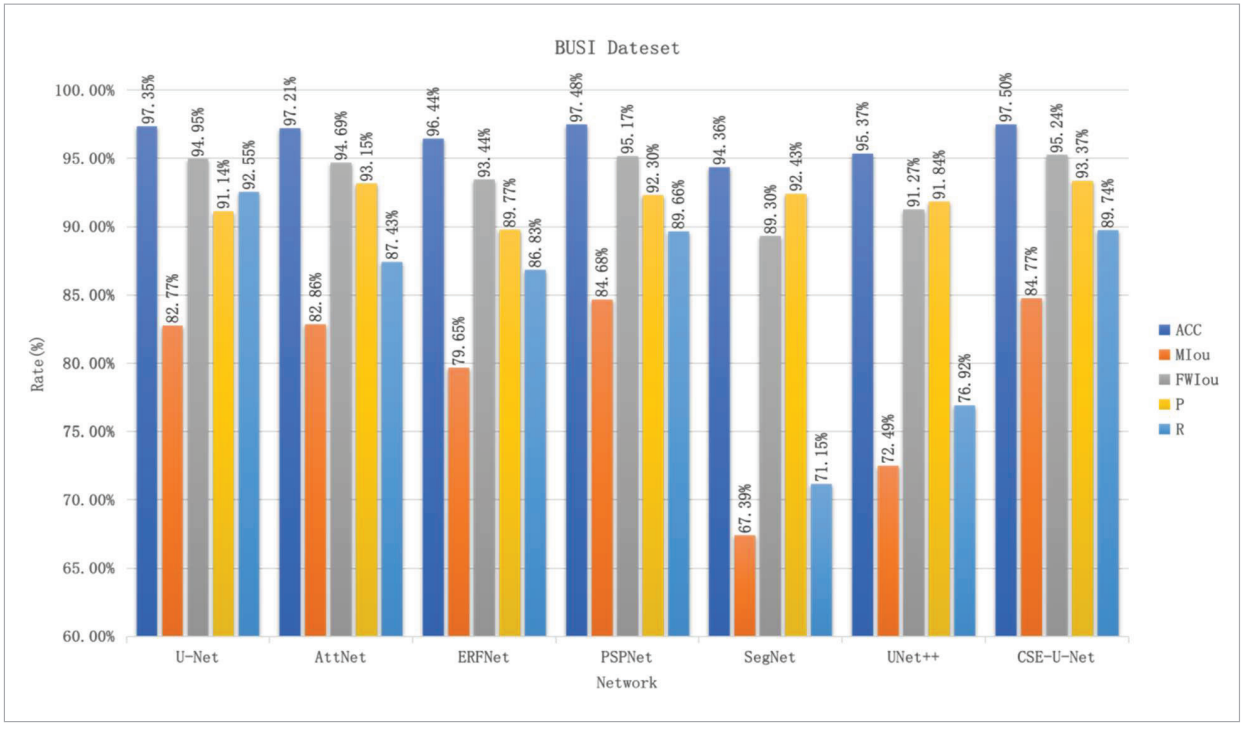

age segmentation. Zhao et al. [41] proposes using a pyramid pooling module structure that integrates multi-scale image features. However, the CSE-U-Net algorithm uses a similar multi-scale fusion method. Figure 11 presents the evaluation index results of the different algorithms on the BUSI dataset. The CSE-U-Net model demonstrated the best results in the five evaluation indexes. Moreover, PSPNet still achieved good results, coming only second to CSE-U-Net, which was significantly improved compared with UNet++ (Acc increased by 2.13%, MIou increased by 12.28%, and FWIou increased by 3.97%). This shows that the CSE-U-Net model is effective in extracting image spatial and context semantic information.

Four breast ultrasound images were randomly selected from the test sets of XJBUSI and BUSI. Images were segmented using U-Net, AttNet, ERFNet, PSPNet, SegNet, UNet++, and CSE -U-Net. The segmentation results are presented in Figure 12. In the segmented images, black represents the background, white represents the malignant tumor area, and green represents the benign tumor area. As shown in the segmented result graph, the SegNet network had the worst segmentation effect. It has insufficient shape fit and poor edge detection ability in breast ultrasound images. The PSPNet network is closest to the CSE-U-Net model; however, its ability to extract edge information is insufficient.

Among the tested many models, the proposed CSE-U-Net model demonstrated the best segmentation effect and stronger robustness. The breast tumor morphology information was extracted most completely in the segmented results, the shape was more consistent with the label, and the segmented tumor edges were smoother and more accurate compared with the other models.

3.4.2. Radiomics Experiments and Analysis

In this study, 300 TNBC and NTNBC breast ultrasound images were extracted through radiomics. The most important 8 features were extracted from 465 features using the Student's t test and LASSO methods on high-dimensional feature data, such as the filtered features, coefficients and t-score reported in Table 3. When feature filtering is performed for the LASSO method in Figure 13, Figure 13(a) shows that the MSE changes with the penalty factor Lambda of the penalty function, and when Lambda=0.005, the MSE gets the minimum value, where the weight w is the optimal value. As shown in Figure 13(b), as lambda increases, the eigenvalue compression decreases; accordingly, the coefficients gradually decrease to 0. The larger the opening curve is, the more obvious the coefficient compression becomes with increasing lambda.

Figure 12

Comparison between tumor segmentation results.

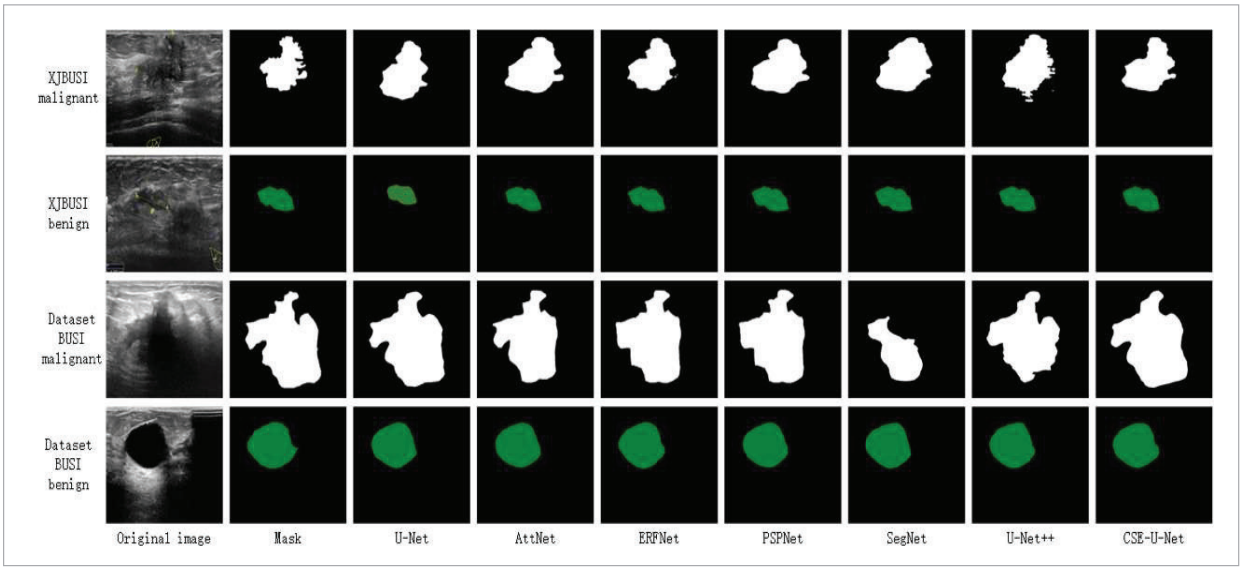

Table 3
Radiomics important features.

Features	Coefficients	t-score
wavelet.HL_glcm_MCC	-0.116740806	8.502
wavelet.LH_glrlm_ShortRunEmphasis	-0.063200052	6.658
wavelet.LL_glszm_ZoneEntropy	-0.062976636	-6.692
wavelet.HH_gldm_SmallDependenceLowGrayLevelEmphasis	-0.073042477	-5.825
wavelet.LH_glrlm_RunLengthNonUniformityNormalized	0.065649188	8.02
wavelet.HH_firstorder_Range	0.129828916	9.24
wavelet.LH_glrlm_ShortRunHighGrayLevelEmphasis	0.066503545	6.658
wavelet.HH_glszm_SmallAreaHighGrayLevelEmphasis	0.098885515	5.122w

Figure 13
Diagram of the coefficient variation with lambda parameters.

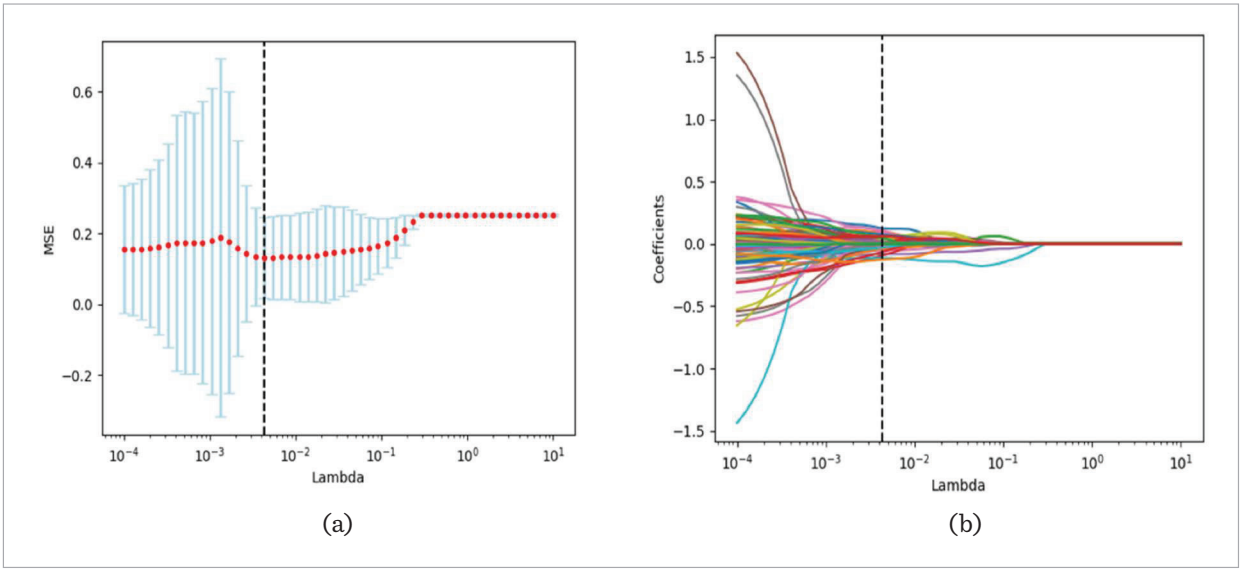

(a) (b)

Finally, the 25 most important image features extracted were modeled using the Random Forest (RF) [7], Support Vector Machine (SVM)[30], extreme Gradient Boosting (XGB)[9], Light Gradient Boosting Machine (LightGBM) [17], logistic [32] algorithms and CNN[11] presented in Table 4, which reports the experimental results of TNBC and NTNBC classification.

As shown in Table 4, the best performance of MSE and Acc is XGB model, reaching 17.78% and 82.22%, respectively. The best performance model for Sensitivity was CNN, reaching 98.46%; Specificity was the best performing SVM model, reaching 54.54%; The best performance model of the comprehensive index F1-score is random forest. The ROC curves for each model are shown in Figure 14. After a thorough comparison, one can observe that the logistic model had the largest AUC area and best overall effect. Sensitivity is of great importance in the field of medical imaging diagnosis. Sensitivity indicates the proportion of patients correctly diagnosed to the total number of patients and is a key indicator to eval-

Table 4
TNBC and NTNBC experimental results.

Algorithm	MSE	Accuracy	Sensitivity	Specificity	F1-Score	Train_AUC	Test_AUC
RF	21.11%	78.89%	83.67%	82.93%	84.54%	100%	90.77%
SVM	24.44%	75.56%	67.35%	95.12%	78.57%	88.59%	83.18%
XGB	17.78%	82.22%	79.59%	85.37%	82.98%	100%	89.10%
LightGBM	22.22%	77.78%	71.43%	92.68%	80.46%	100%	89.25%
Logistic	21.11%	78.89%	75.51%	87.8%	81.32%	93.74%	90.89%
CNN	44.00%	78.33%	98.46%	54.54%	60.70%	82.09%	82.08%

uate the diagnostic effect. Specificity indicates the percentage of patients who are correctly diagnosed as disease-free. Specificity is more meaningful to patients than Sensitivity. Due to the limitation of the number of pictures, CNN is not ideal in the task of classification of TNBC and NTNBC. Although CNN performs well on the Sensitivity index, it does not perform as well on the Specificity and F1-Score index as other algorithms. Therefore, this paper classifies triple-negative and non-triple-negative breast cancer using imaging histology.

The experimental results indicate that the CSE-U-Net model can automatically identify benign and malignant tumor categories and extract tumor regions and locations, which lays a good foundation for radiomics feature extraction. To better classify malignant TNBC and NTNBC, we used the image histology method to extract the tumor feature information of breast ultrasound images, screen for the high-dimensional features, and reduce the dimensionality. Finally, five machine learning algorithms were used to classify malignant tumors with an accuracy of more than 75.56%.

Figure 14
ROC curves for each model.

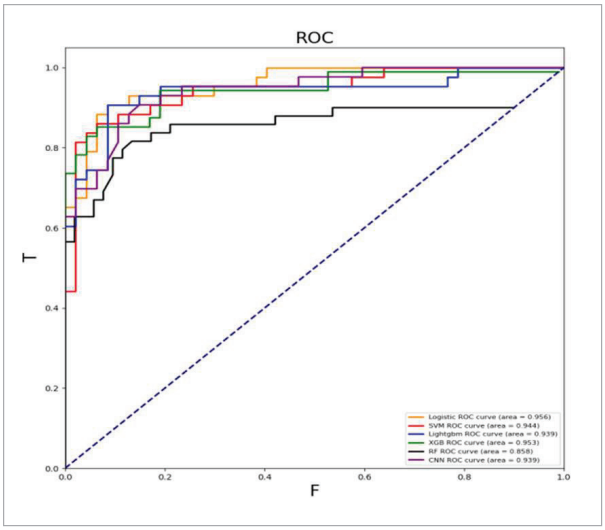

4. Conclusion

In this study, we mainly investigated the classification method of TNBC and NTNBC. First, we proposed an improved CSE-U-Net model. By combining the multi-scale channel attention and spatial awareness modules, the impact of different tumor scales on tumor information extraction is weakened, which enhances the robustness and improves the accuracy of tumor detection. The ECA attention mechanism is added to improve the feature extraction ability of the model from tumor edges, making the segmented tumor edges smoother. Benign and malignant tumor segmentation and classification tests were conducted on XJBUSI and BUSI datasets. The main indicators, such as Acc and MIou, were higher than those of other comparison models, and the segmented images are extracted with radiomics features. In addition, using a machine learning model to classify TNBC and NTNBC, the accuracy of the XGB model with the highest accuracy reached 82.22%. The experimental results show that the proposed segmentation model and classification method have high segmentation and classification accuracy; however, there remains a segmentation speed issue. Therefore, in the future,

we can consider introducing lightweight feature extraction deep learning network to improve the model segmentation speed and further improve the overall model performance of the model. Regarding radiomics, we analyzed the characteristics of multimodality and multi-factors to improve the classification accuracy regarding TNBC and NTNBC in ultrasound images.

Funding

This work was supported by the Xinjiang Urumqi Hongshan Science and Technology Innovation Young Talents Program (B241013006) and Tianshan Talent of Xinjiang Uygur Autonomous Region-Young Top Talents in Science and Technology under Grant 2022TSYCCY0008.

References

1. Al-Dhabyani, W., Gomaa, M., Khaled, H., Fahmy, A. Dataset of Breast Ultrasound Images. Data in Brief, 2023, 48, 109247. doi:10.1016/j.dib.2019.104863 https://doi.org/10.1016/j.dib.2019.104863
2. Anand, A., Jung, S., Lee, S. Breast Lesion Detection for Ultrasound Images Using MaskFormer. Sensors (Basel), 2024, 24(21), 6890. doi:10.3390/s24216890 https://doi.org/10.3390/s24216890
3. Avdan Aslan, A., Gültekin, S., Karakoç, E., Tosun, S. N. Impact of Menopausal Status on Imaging Findings of Patients with Triple-Negative Breast Cancer. Journal of Breast Imaging, 2022, 4(4), 384-391. doi:10.1093/jbi/wbac027
4. Azamjah, N., Soltan-Zadeh, Y., Zayeri, F. Global Trend of Breast Cancer Mortality Rate: A 25-Year Study. Asian Pacific Journal of Cancer Prevention, 2019, 20(7), 2015-2020. doi:10.31557/APJCP.2019.20.7.2015 https://doi.org/10.31557/APJCP.2019.20.7.2015
5. Badrinarayanan, V., Kendall, A., Cipolla, R. SegNet: A Deep Convolutional Encoder-Decoder Architecture for Image Segmentation. IEEE Transactions on Pattern Analysis and Machine Intelligence, 2017, 39(12), 2481-2495. doi:10.1109/TPAMI.2016.2644615 https://doi.org/10.1109/TPAMI.2016.2644615
6. Bertozzi, S., Londero, A. P., Diaz Nanez, J. A., Di Vora, R., Baita, B., La Verghetta, L., Prada, S., Seriau, L., Mariuzzi, L., Cedolini, C. Breast Cancer Care for the Aging Population: A Focus on Age-Related Disparities in Breast Cancer Treatment. BMC Cancer, 2025, 25(1), 492. doi:10.1186/s12885-025-13893-8 https://doi.org/10.1186/s12885-025-13893-8
7. Breiman, L. Random Forests. Machine Learning, 2021, 45, 5-32. http://dx.doi.org/10.1023/A:1010933404324 https://doi.org/10.1023/A:1010933404324
8. Cai, L., Sidey-Gibbons, C., Nees, J., Riedel, F., Schaefgen, B., Togawa, R., Killinger, K., Heil, J., Pfob, A., Golatta, M. Ultrasound Radiomics Features to Identify Patients with Triple-Negative Breast Cancer: A Retrospective, Single-Center Study. Journal of Ultrasound in Medicine, 2024, 43(3), 467-478. doi:10.1002/jum.16377 https://doi.org/10.1002/jum.16377
9. Chen, T., Guestrin, C. XGBoost: A Scalable Tree Boosting System. Proceedings of the ACM SIGKDD International Conference on Knowledge Discovery and Data Mining, 2016. doi:10.1145/2939672.2939785 https://doi.org/10.1145/2939672.2939785
10. Ching, T., Himmelstein, D. S., Beaulieu-Jones, B. K., Kalinin, A. A., Do, B. T., Way, G. P., Ferrero, E., Agapow, P. M., Zietz, M., Hoffman, M. M., Xie, W., Rosen, G. L., Lengerich, B. J., Israeli, J., Lanchantin, J., Woloszynek, S., Carpenter, A. E., Shrikumar, A., Xu, J., Cofer, E. M., Lavender, C. A., Turaga, S. C., Alexandari, A. M., Lu, Z., Harris, D. J., DeCaprio, D., Qi, Y., Kundaje, A., Peng, Y., Wiley, L. K., Segler, M. H. S., Boca, S. M., Swamidass, S. J., Huang, A., Gitter, A., Greene, C. S. Opportunities and Obstacles for Deep Learning in Biology and Medicine. Journal of the Royal Society Interface, 2018, 15(141), 20170387. doi:10.1098/rsif.2017.0387 https://doi.org/10.1098/rsif.2017.0387
11. Gao, C., Li, X., Zhou, F., Mu, S. Face Liveness Detection Based on the Improved CNN With Context and Texture Information. Chinese Journal of Electronics, 2019, 28(6), 1092-1098. doi:10.1049/cje.2019.07.012 https://doi.org/10.1049/cje.2019.07.012
12. Gu, Y., Xu, W., Lin, B., An, X., Tian, J., Ran, H., Ren, W., Chang, C., Yuan, J., Kang, C., Deng, Y., Wang, H., Luo, B., Guo, S., Zhou, Q., Xue, E., Zhan, W., Zhou, Q., Li, J., Zhou, P., Chen, M., Gu, Y., Chen, W., Zhang, Y., Li, J., Cong, L., Zhu, L., Wang, H., Jiang, Y. Deep Learning Based on Ultrasound Images Assists Breast Lesion Diagnosis in China: A Multicenter Diagnostic Study. Insights into Imaging, 2022, 13(1), 124. doi:10.1186/s13244-022-01259-8 https://doi.org/10.1186/s13244-022-01259-8

13. Guizani, S., Guizani, N., Gharsallaoui, S. A Hybrid CNN-SVM Prediction Approach for Breast Cancer Ultrasound Imaging. 2023 International Wireless Communications and Mobile Computing Conference (IWCMC), Marrakesh, Morocco, 2023, 1574-1578. doi:10.1109/IWCMC58020.2023.10182874 https://doi.org/10.1109/IWCMC58020.2023.10182874

14. Habashi, A. G., Azab, A. M., Eldawlatly, S., Aly, G. M. Generative Adversarial Networks in EEG Analysis: An Overview. Journal of NeuroEngineering and Rehabilitation, 2023, 20(1), 40. doi:10.1186/s12984-023-01169-w https://doi.org/10.1186/s12984-023-01169-w

15. Hu, J., Shen, L., Albanie, S., Sun, G., Wu, E. Squeeze-and-Excitation Networks. IEEE Transactions on Pattern Analysis and Machine Intelligence, 2020, 42(8), 2011-2023. doi:10.1109/TPAMI.2019.2913372 https://doi.org/10.1109/TPAMI.2019.2913372

16. Ibtehaz, N., Rahman, M. S. MultiResUNet: Rethinking the U-Net Architecture for Multimodal Biomedical Image Segmentation. Neural Networks, 2020, 121, 74-87. doi:10.1016/j.neunet.2019.08.025 https://doi.org/10.1016/j.neunet.2019.08.025

17. Ke, G., Meng, Q., Finley, T., Wang, T., Chen, W., et al. LightGBM: A Highly Efficient Gradient Boosting Decision Tree. Proceedings of the 31st International Conference on Neural Information Processing Systems (NeurIPS), 2017, Long Beach, United States. ffhal-03953007. https://hal.science/hal-03953007v1

18. Lambin, P., Rios-Velazquez, E., Leijenaar, R., Carvalho, S., van Stiphout, R. G., Granton, P., Zegers, C. M., Gillies, R., Boellard, R., Dekker, A., Aerts, H. J. Radiomics: Extracting More Information from Medical Images Using Advanced Feature Analysis. European Journal of Cancer, 2012, 48(4), 441-446. doi:10.1016/j.ejca.2011.11.036 https://doi.org/10.1016/j.ejca.2011.11.036

19. Li, D., Duan, Q. A New Prediction Model of Triple-Negative Breast Cancer Based on Ultrasound Radiomics. European Journal of Gynaecological Oncology, 2025, 46(4), 64-72. doi:10.22514/ejgo.2025.052 https://doi.org/10.22514/ejgo.2025.052

20. Oktay, O., Schlemper, J., Folgoc, L. L., Lee, M., Heinrich, M., Misawa, K., Mori, K., McDonagh, S., Hammerla, N. Y., Kainz, B. Attention U-Net: Learning Where to Look for the Pancreas. 2018. https://doi.org/10.48550/arXiv.1804.03999

21. Othman Abdullah, M., Altun, Y., Maghded Ahmed, R. Leveraging Artificial Neural Networks and Support Vector Machines for Accurate Classification of Breast Tumors in Ultrasound Images. Cureus, 2024, 16(11), e73067. doi:10.7759/cureus.73067 https://doi.org/10.7759/cureus.73067

22. Ramola, A., Shakya, A. K., Pham, D. V. Study of Statistical Methods for Texture Analysis and Their Modern Evolutions. Engineering Reports, 2020, 2(4), e12149. doi:10.1002/eng2.12149 https://doi.org/10.1002/eng2.12149

23. Rao, K. S., Terlapu, P. V., Jayaram, D., Raju, K. K., Kumar, G. K., Pemula, R., Gopalachari, M. V., Rakesh, S. Intelligent Ultrasound Imaging for Enhanced Breast Cancer Diagnosis: Ensemble Transfer Learning Strategies. IEEE Access, 2024, 12, 22243-22263. doi:10.1109/ACCESS.2024.3358448 https://doi.org/10.1109/ACCESS.2024.3358448

24. Romera, E., Álvarez, J. M., Bergasa, L. M., Arroyo, R. ERFNet: Efficient Residual Factorized ConvNet for Real-Time Semantic Segmentation. IEEE Transactions on Intelligent Transportation Systems, 2018, 19(1), 263-272. doi:10.1109/TITS.2017.2750080 https://doi.org/10.1109/TITS.2017.2750080

25. Ronneberger, O., Fischer, P., Brox, T. U-Net: Convolutional Networks for Biomedical Image Segmentation. In Medical Image Computing and Computer-Assisted Intervention - MICCAI 2015, Cham, 2015. Springer International Publishing, 234-241. https://doi.org/10.48550/arXiv.1505.04597 https://doi.org/10.1007/978-3-319-24574-4_28

26. Ru, J., Zhu, Z., Shi, J. Spatial and Geometric Learning for Classification of Breast Tumors from Multi-Center Ultrasound Images: A Hybrid Learning Approach. BMC Medical Imaging, 2024, 24(1), 133. doi:10.1186/s12880-024-01307-3 https://doi.org/10.1186/s12880-024-01307-3

27. Santosh, N. K., Barpanda, S. S. Wavelet Applications in Medical Image Processing. In Predictive Intelligence in Biomedical and Health Informatics, De Gruyter, 2020, 63-90. https://ieeexplore.ieee.org/document/10789403 https://doi.org/10.1515/9783110676129-004

28. Shahabaz, D. K., Somwanshi, A. K., Yadav, R., Roy, R. Medical Images Texture Analysis: A Review. 2017 International Conference on Computer, Communications and Electronics (Comptelix), Jaipur, India, 2017, 436-441. doi:10.1109/COMPTELIX.2017.8004009 https://doi.org/10.1109/COMPTELIX.2017.8004009

29. Shelhamer, E., Long, J., Darrell, T. Fully Convolutional Networks for Semantic Segmentation. IEEE Transactions on Pattern Analysis and Machine Intelligence, 2017, 39(4), 640-651. doi:10.1109/TPAMI.2016.2572683 https://doi.org/10.1109/TPAMI.2016.2572683

30. Suykens, J. A. K., Vandewalle, J. Least Squares Support Vector Machine Classifiers. Neural Processing Letters, 1999, 9, 293-300. doi:10.1023/A:1018628609742 https://doi.org/10.1023/A:1018628609742

31. Sung, H., Ferlay, J., Siegel, R. L., Laversanne, M., Soerjomataram, I., Jemal, A., Bray, F. Global Cancer Statistics 2020: GLOBOCAN Estimates of Incidence and Mortality Worldwide for 36 Cancers in 185 Countries. CA: A Cancer Journal for Clinicians, 2021, 71(3), 209-249. doi:10.3322/caac.21660 https://doi.org/10.3322/caac.21660

32. Tong, X., Wei, J., Sun, B., Su, S., Zuo, Z., Wu, P. ASCU-Net: Attention Gate, Spatial and Channel Attention U-Net for Skin Lesion Segmentation. Diagnostics (Basel), 2021, 11(3), 501. doi:10.3390/diagnostics11030501 https://doi.org/10.3390/diagnostics11030501

33. Vourtsis, A. Three-Dimensional Automated Breast Ultrasound: Technical Aspects and First Results. Diagnostic and Interventional Imaging, 2019, 100(10), 579-592. doi:10.1016/j.diii.2019.03.012 https://doi.org/10.1016/j.diii.2019.03.012

34. Wan, Y., Yang, Y., Guo, H., Yan, Y., Liu, T., Liu, W., Wang, Y., Wang, W., Dang, H. D-TransUNet: A Breast Tumor Ultrasound Image Segmentation Model Based on Deep Feature Fusion. Journal of Artificial Intelligence for Medical Sciences, 2024, 5(1), 1-8. doi:10.55578/joaims.240226.001 https://doi.org/10.55578/joaims.240226.001

35. Wang, Q., Wu, B., Zhu, P., Li, P., Zuo, W., Hu, Q. ECA-Net: Efficient Channel Attention for Deep Convolutional Neural Networks. 2020 IEEE/CVF Conference on Computer Vision and Pattern Recognition (CVPR), Seattle, WA, USA, 2020, pp. 11531-11539. doi:10.1109/CVPR42600.2020.01155 https://doi.org/10.1109/CVPR42600.2020.01155

36. Wenwen, W., Jiang, Z., Liu, J., Liu, D., Li, Y., He, Y., Zhao, H., Ma, L., Zhu, Y., Long, Q., Gao, J., Luo, H., Jiang, H., Li, K., Zhong, X., Peng, Y. Integrating Ultrasound Radiomics and Clinicopathological Features for Machine Learning-Based Survival Prediction in Patients with Nonmetastatic Triple-Negative Breast Cancer. BMC Cancer, 2025, 25(1), 291. doi:10.1186/s12885-025-13635-w https://doi.org/10.1186/s12885-025-13635-w

37. Yamada, M., Jitkrittum, W., Sigal, L., Xing, E. P., Sugiyama, M. High-Dimensional Feature Selection by Feature-Wise Kernelized Lasso. Neural Computation, 2014, 26(1), 185-207. doi:10.1162/NECO_a_00537 https://doi.org/10.1162/NECO_a_00537

38. Ye, Z., Kumar, Y. J., Song, F., Li, G., Zhang, S. Bi-DCNet: Bilateral Network with Dilated Convolutions for Left Ventricle Segmentation. Life (Basel), 2023, 13(4), 1040. doi:10.3390/life13041040 https://doi.org/10.3390/life13041040

39. Yun, S., Toh, K.-C. A Coordinate Gradient Descent Method for l1-Regularized Convex Minimization. Computational Optimization and Applications, 2011, 48(2), 273-307. doi:10.1007/s10589-009-9251-8 https://doi.org/10.1007/s10589-009-9251-8

40. Zill, D. G., Wright, W. S. Advanced Engineering Mathematics. 5th ed., Wiley.

41. Zhao, H., Shi, J., Qi, X., Wang, X., Jia, J. Pyramid Scene Parsing Network. 2017 IEEE Conference on Computer Vision and Pattern Recognition (CVPR), Honolulu, HI, USA, 2017, 6230-6239. doi:10.1109/CVPR.2017.660 https://doi.org/10.1109/CVPR.2017.660

42. Zhou, Z., Siddiquee, M. M. R., Tajbakhsh, N., Liang, J. UNet++: A Nested U-Net Architecture for Medical Image Segmentation. Deep Learning in Medical Image Analysis and Multimodal Learning for Clinical Decision Support, 2018, 11045, 3-11. doi:10.1007/978-3-030-00889-5_1 https://doi.org/10.1007/978-3-030-00889-5_1

43. Zhang, Y., Ngo, H. C., Zhang, Y., Yusof, N. F. A., Wang, X. Imaging Segmentation of Brain Tumors Based on the Modified U-Net Method. Information Technology and Control, 2024, 53(4), 1074-1087. https://doi.org/10.5755/j01.itc.53.4.37719 https://doi.org/10.5755/j01.itc.53.4.37719

44. Zhou, X., Ma, J., Yi, J. CSST-Net: Channel Split Spatiotemporal Network for Human Action Recognition. Information Technology and Control, 2023, 52(4), 952-965. https://doi.org/10.5755/j01.itc.52.4.33239 https://doi.org/10.5755/j01.itc.52.4.33239